Magnetic Stress-Driven Metal-Insulator Transition in Strongly Correlated Antiferromagnetic CrN

Bidesh Biswas,[1,2] Sourav Rudra,[1,2] Rahul Singh Rawat,[1,2] Nidhi Pandey,[1,2] Shashidhara Acharya,[1,2] Anjana Joseph,[1,2] Ashalatha Indiradevi Kamalasanan Pillai,[3] Manisha Bansal,[4] Muireann de h-Óra,[5] Debendra Prasad Panda,[1,8] Arka Bikash Dey,[6] Florian Bertram,[6] Chandrabhas Narayana,[1,7] Judith MacManus-Driscoll,[5] Tuhin Maity,[4] Magnus Garbrecht,[3] and Bivas Saha[1,2,8,*]

[1]*Chemistry and Physics of Materials Unit, Jawaharlal Nehru Centre for Advanced Scientific Research, Bangalore 560064, India*
[2]*International Centre for Materials Science, Jawaharlal Nehru Centre for Advanced Scientific Research, Bangalore 560064, India*
[3]*Sydney Microscopy and Microanalysis, The University of Sydney, Camperdown, NSW 2006, Australia*
[4]*School of Physics, Indian Institute of Science Education and Research Thiruvananthapuram, Thiruvananthapuram, Kerala 695551, India*
[5]*Department of Materials Science and Metallurgy, University of Cambridge, CB3 OFS Cambridge, United Kingdom*
[6]*Deutsches Elektronen-Synchrotron (DESY), Hamburg 22607, Germany*
[7]*Rajiv Gandhi Centre for Biotechnology, Poojappura, Thiruvananthapuram 695014, India*
[8]*School of Advanced Materials and Sheikh Saqr Laboratory, Jawaharlal Nehru Centre for Advanced Scientific Research, Bangalore 560064, India*

(Received 22 November 2022; revised 12 May 2023; accepted 23 August 2023; published 22 September 2023)

Traditionally, the Coulomb repulsion or Peierls instability causes the metal-insulator phase transitions in strongly correlated quantum materials. In comparison, magnetic stress is predicted to drive the metal-insulator transition in materials exhibiting strong spin-lattice coupling. However, this mechanism lacks experimental validation and an in-depth understanding. Here we demonstrate the existence of the magnetic stress-driven metal-insulator transition in an archetypal material, chromium nitride. Structural, magnetic, electronic transport characterization, and first-principles modeling analysis show that the phase transition temperature in CrN is directly proportional to the strain-controlled anisotropic magnetic stress. The compressive strain increases the magnetic stress, leading to the much-coveted room-temperature transition. In contrast, tensile strain and the inclusion of nonmagnetic cations weaken the magnetic stress and reduce the transition temperature. This discovery of a new physical origin of metal-insulator phase transition that unifies spin, charge, and lattice degrees of freedom in correlated materials marks a new paradigm and could lead to novel device functionalities.

DOI: 10.1103/PhysRevLett.131.126302

Ever since the first observation of the Verwey transition [1] of magnetite in 1939, the metal-insulator phase transition (MIT) has captivated generations of scientists and engineers for fundamental scientific knowledge and expansive device applications [2–6]. Traditionally, MIT in most well-established quantum materials is governed by the Mott-Hubbard mechanism, where strong electronic repulsion in transition metals drives the system from metallic to an insulating state [7–9]. In addition, structural instability (Peierls transition) and the presence of lattice defects or disorders (Anderson transition) are also known to cause MIT in some materials [10–14]. Concomitant with the MIT, strongly correlated materials can also undergo structural and magnetic phase transition due to their coupled spin, charge, and lattice degrees of freedom [15–18]. However, as the aforementioned mechanisms explain the origin of the phase transition as driven by a single or double order parameter [19–21] (either electronic and/or structural), independent control of the MIT with other degrees of freedom such as magnetic ordering or structural symmetry is challenging.

Recent theoretical modeling has predicted that materials exhibiting strong spin-lattice coupling could be the host of a new type of MIT accompanied by simultaneous structural and magnetic phase transition [22–26]. Non-spin-polarized-to-spin-polarized magnetic ordering is expected to generate an anisotropic magnetic stress that changes its structure and the electronic phase. Such a magnetic stress-driven phase transition mechanism which unifies the magnetic, mechanical, and electrical order parameters in correlated materials offers much freedom to achieve tunable properties in a single material system. Besides, since the Coulomb repulsion or Peierls instability-driven phase transition mechanism is mainly observed in transition metal oxides and sulfides [27–29], the new transition mechanism could also lead to a plethora of new materials exhibiting the MIT, such as the nitride pnictides, antiperovskites, etc. Therefore,

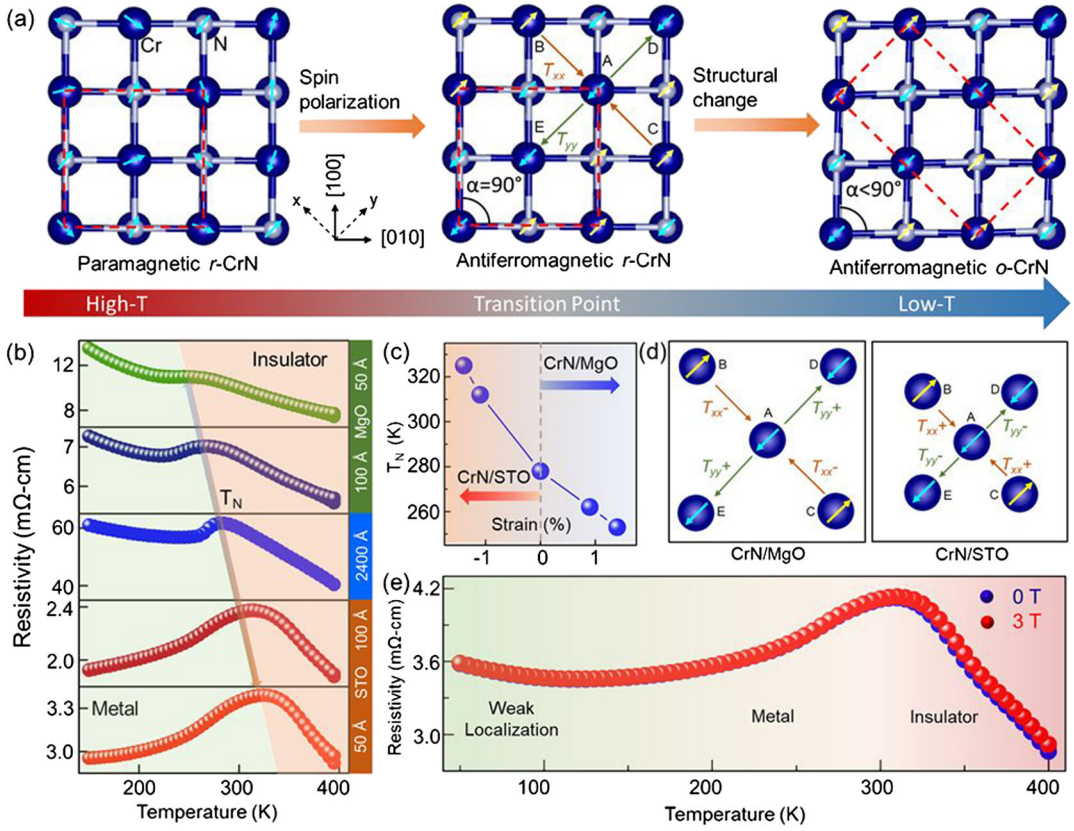

FIG. 1. (a) Schematic showing a nonspin polarized to AFM non spin-polarized transition accompanied with the structural transition in CrN. After the initial spin polarization, a compressive magnetic-stress T_{xx} and tensile magnetic-stress T_{yy} distort the cubic structural symmetry and transform it into an orthorhombic structure. (b) Temperature-dependent resistivity of relaxed (blue) and strained films shows that compressive stress increases the T_N, while tensile stress decreases T_N in CrN. (c) The evolution of transition temperature with in-plane strain shows a linear behavior. (d) Schematic description of the changes in magnetic stress in CrN with epitaxial strain. The T_{xx} decreases (T_{xx}^{-}), and increases (T_{xx}^{+}) in tensile and compressively strained films, respectively. The T_{yy} behaves conversely to T_{xx}. (e) Temperature-dependent electrical resistivity of 10 nm CrN on STO substrate at two different out-of-plane magnetic fields of 0 and 3 T.

experimental observation of the magnetic stress-driven MIT and its manipulation is of great interest.

To study the magnetic stress-driven MIT, we choose archetypal material chromium nitride (CrN) that exhibits large magnetic stress, as predicted by the density functional theory [22,23,30]. CrN is paramagnetic at high temperature and becomes antiferromagnetic (AFM) below the Néel temperature $(T_N) \approx 271$–280 K [31–36]. Concomitant to the magnetic transition, the structural symmetry changes from the rocksalt ($Fm\bar{3}$m) at high temperature to orthorhombic (P_{nma}) below T_N. Such simultaneous magnetic and structural phase change is accompanied by the electronic transition from the high-temperature insulating phase to the low-temperature metallic phase. It contrasts the nature of MIT described by Mott, Anderson, and Peierls-transition mechanisms, where the metallic phase at high-temperature changes to the insulating phase at low temperature.

MIT in CrN was modeled theoretically in terms of the anisotropic magnetic stress [23,24]. The magnetic-stress T in a system is defined as the stress associated with the change of spin ordering. For two different magnetic orderings O^1 and O^2, the magnetic stress can be expressed as $T = T^{O^1} - T^{O^2}$, which can be further mapped to the magnetic stress per bond as $T = -\boldsymbol{S}_i.\boldsymbol{S}_j t_{ij}$, where $\boldsymbol{S}$ is the spin matrix of the ith and jth site atom and t_{ij} is the stress tensor, related to the exchange interaction parameter J_{ij} between the atoms. In case of CrN, the magnetic stress appears around the transition point T_N. Cooling down the paramagnetic CrN results in polarization of the individual spin in an unusual antiferromagnetic ordering ($\mathrm{AFM}^2_{[1\bar{1}0]}$) where two ferromagnetic (FM) layers alternate along the $[1\bar{1}0]$ direction of the rocksalt CrN [37–39] [Fig. 1(a)]. Because of this unusual spin ordering, the Cr atoms in rocksalt CrN are subjected to two different stress. In Fig. 1(a), the Cr-A atom has two neighboring atoms (Cr-B and Cr-C) with opposite spins and two neighboring atoms (Cr-D and Cr-E) with similar spins. As a result, the Cr-A atom is subjected to compressive stress (T_{xx}) along the $\boldsymbol{x}$ direction and tensile stress (T_{yy}) along the $\boldsymbol{y}$ direction. This anisotropic stress is relieved by the lattice contraction along the $\boldsymbol{x}$ direction and lattice expansion along the

y direction, which changes the crystal symmetry of CrN from rocksalt-to-orthorhombic. Subsequently, the electronic phase changes from insulating to metallic. Thus, the magnetic stress-driven phase transition mechanism in CrN not only explains the origin of MIT but also suggests a method to tune the transition temperature through the manipulation of magnetic stress.

Despite the theoretical prediction, experimental validation of the transition mechanism is still lacking. Though efforts have been made using photoemission spectroscopy to understand the electronic nature of the two different phases, as well as to understand the strain and size-induced changes in the electrical resistivity, no conclusive work has been performed to demonstrate the magnetic stress-driven phase transition mechanism experimentally [35,40]. As the anisotropic magnetic stress due to magnetic exchange-interaction in CrN is relatively low, experimental control and manipulation of such interactions are extremely challenging. Furthermore, depositing phase-pure single-crystalline CrN thin films that exhibit MIT is very difficult [41–45], which has further hindered the exploration of phase transition phenomena in CrN for a long time. However, recent experimental work [43,46] has shown that by utilizing a very small Cr-flux during deposition and with suitable growth temperature, phase-pure single-crystalline CrN thin films can be obtained that reproducibly exhibit the MIT. Given that the deposition conditions of CrN thin film that shows MIT are now well-developed, the hypothesis of the magnetic stress-driven MIT could be verified. Here we consider the epitaxial strain and the inclusion of substitutional non-magnetic cations as two different means to manipulate the magnetic stress.

To this end, we deposited biaxial compressive and tensile-strained single-crystalline CrN thin films on (001) $SrTiO_3$ (STO) and (001) MgO substrates, respectively. As CrN has an equilibrium lattice constant of 4.15 Å, it exhibits a lattice-mismatch of $\sim -5.9\%$ with (001) STO and ∼1.4% with (001) MgO substrates. Film thicknesses are limited to less than 10 nm to prevent strain relaxation due to plastic deformation. Relaxed (001) CrN with 240 nm thickness is further deposited separately.

The temperature-dependent electrical resistivity measurements show that the relaxed 240 nm CrN thin film exhibit MIT at ∼278 K accompanied by a hysteresis of ∼2 K between the heating and cooling cycles [Fig. 1(b)]. The hysteresis temperature is quite robust irrespective of the changes in the heating and cooling rates (Fig. S4 in Supplemental Material [47]). Starting from ∼235 K up to the MIT point ($T_N \sim 278$ K [33,48]), resistivity increases with the increase in temperature, highlighting the metallic behavior of CrN. However, the resistivity decreases with increasing temperature after the MIT point, clearly showing the high-temperature semiconducting nature.

Compared to the relaxed film, ultrathin 10 and 5 nm CrN deposited on STO substrate exhibit MIT at ∼312 and ∼325 K [Fig. 1(b), S5], respectively. The compressive strained films exhibit a hysteresis of ∼2–3 K, further ensuring their first-order MIT behavior. In contrast, tensile strained 10 and 5 nm CrN films deposited on MgO substrate exhibit MIT at ∼262 and ∼253 K, respectively. Since the amount of tensile or compressive strain stored in a 5 nm CrN is larger than that in a 10 nm film due to strain relaxation with increased thickness, the measured phase transition temperature correlates with the sign and amount of strain in the films. A plot of the phase transition temperature with film thickness or strain shows [Fig. 1(c)] a linear behavior. Thus, through controlled strain engineering, a desired MIT temperature from ∼253 to ∼325 K can be achieved in CrN. Away from the MIT point, at low temperatures, all the CrN films exhibit an increase in resistivity with the decrease in temperature (Fig. S5 [47]) due to weak electronic localization.

The increase or decrease in T_N of CrN on STO/MgO substrates can be explained in terms of the changes in magnetic stress due to epitaxial strain [Fig. 1(d)]. In the case of CrN film deposited on STO substrate, the compressive epitaxial strain shortens the in-plane Cr-Cr distance compared to the Cr-Cr distance in a relaxed film. As a result, the AFM exchange-interaction along the *x* direction increases, resulting in rocksalt-to-orthorhombic structural transformation at higher temperatures. In comparison, for CrN film on MgO substrate, the increased Cr-Cr distance weakens the AFM exchange-interaction, and thus, the transition occurs at a much lower temperature.

Interestingly, the magnetic-field-dependent electrical resistivity of 10 nm CrN/STO shows [Fig. 1(e)] that the resistivity remains unchanged in the metallic region ($T < T_N$) and exhibits a small change (difference of ∼3%) in the insulating regions ($T > T_N$). This is presumably because, in the metallic region, the CrN is AFM, which shields the effects of the external magnetic field on the transport properties. However, as CrN acquires a paramagnetic phase in the insulating region, the transport of carriers is slightly affected by the external magnetic field.

Further, to correlate the electronic properties with magnetic ordering, temperature-dependent magnetization (M-vs-T) of a 10 nm CrN, and exchange-bias (EB) of a 10 nm/10 nm CrN/Mn_3AlN bilayer deposited on STO substrates are measured [49]. Mn_3AlN is a FM antiperovskite nitride that exhibits a high Curie temperature (T_c) of ∼800 K [47,50]. In the M-vs-T measurement at 500 Oe, the moment remains almost constant in the 350–320 K temperature range. However, as the temperature is reduced below ∼320 K, the magnetization increases drastically, which highlights the onset of the magnetic phase transition [Fig. 2(a)]. Note that the negative value at the moment axis is due to the contribution of the diamagnetic STO substrate. An AFM hysteresis curve (M-vs-H) measured at 2 K is shown in the inset of Fig. 2(a). A prominent EB (H_{EB}) ∼ −350 Oe at 2 K and −60 Oe at 50 K is obtained for the

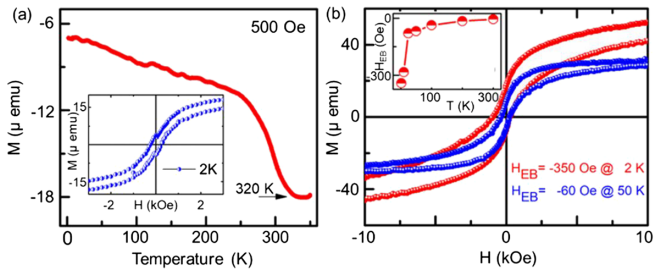

FIG. 2. M-vs-T plot of 10 nm CrN deposited on STO substrate showing the onset of paramagnetic-to-antiferromagnetic transition around 320K. M-vs-H hysteresis curve at 2 K is shown in the inset. (b) Exchange bias in 10 nm/10 nm CrN/Mn_3AlN bilayer system on STO substrate. The temperature-dependent exchange bias is shown in the inset. The exchange bias value increases with the decrease in temperature.

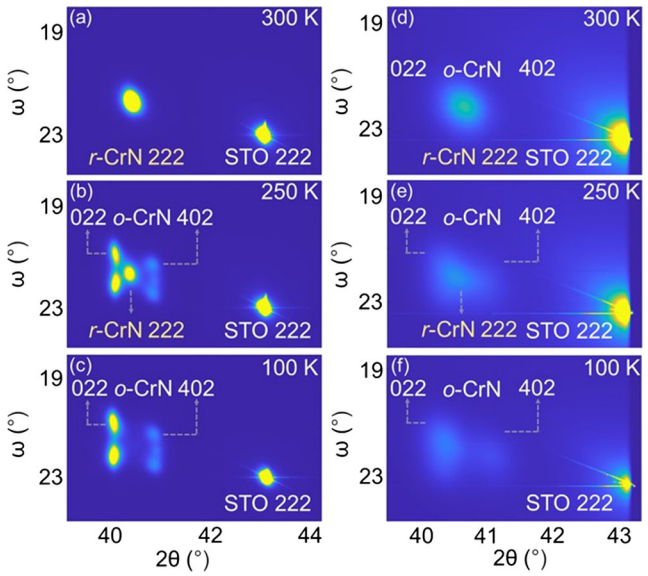

FIG. 3. $\omega - 2\theta$ XRD diffractogram of 240 nm thick relaxed (a)–(c) and 10 nm thick strained (d)–(f) CrN film on STO substrates at 300, 250, and 100 K, respectively. At 300 K, only the rocksalt phase is present. At 250 K, both the rocksalt and orthorhombic phases are present. At 100 K, only the orthorhombic phase is present.

CrN/Mn_3AlN bilayer system [Fig. 2(b)] which proves the AFM nature of CrN. The EB values monotonically increase with the decrease in temperature [Fig. 2(b) inset]. Thus, the combined M-vs-T, M-vs-H, and EB measurements confirm the paramagnetic-to-antiferromagnetic transition around ~320 K in a compressively strained 10 nm CrN film on STO substrate. This magnetic transition correlates with the electrical phase transition at ~312 K observed in the same 10 nm CrN/STO film. Therefore, the strain-induced change in the MIT temperature and the magnetic measurements indicate the presence of a driving force that has a magnetic origin.

Having demonstrated the MIT, the concomitant structural transition is probed with temperature-dependent synchrotron-radiation high-resolution x-ray diffraction (HRXRD) performed at the high-resolution diffraction beam line P08 at PETRA III (DESY) [51]. Structural transition in CrN at T_N from the rocksalt-to-orthorhombic phase involves a reduction in the lattice parameter a $(a_0\sqrt{2})$ and increase in the lattice parameter b $(a_0/\sqrt{2})$ with $a = 2a_0 \sin(\alpha/2)$, $b = a_0 \cos(\alpha/2)$, $c = a_0$ relationship, where $\alpha \approx 88°$ and a_0 is the cubic equilibrium lattice parameters.

At room temperature (300 K), asymmetric $\omega - 2\theta$ HRXRD mapping of relaxed CrN deposited on MgO, and STO substrates show [Fig. 3(a), S8 [47]] two peaks each that correspond to the 222 CrN films and, 222 substrates diffraction spots, respectively. Utilizing Bragg's law, CrN lattice parameter of 4.15 Å is calculated in the rocksalt phase on both substrates, which is consistent with literature reports [41,48]. However, as the sample temperature is lowered to 250 K, the rocksalt 222 (r-222) CrN peak at 40.40° splits into the 022 and 402 CrN orthorhombic peaks at ~40.07° and ~40.82°, respectively [Figs. 3(b) and 3(c)]. Subsequent lattice spacing calculations verify the orientation of these orthorhombic peaks due to the structural transition. The compressively strained 10 nm CrN on STO substrate also shows structural transition [Figs. 3(d)–3(f)]. A detailed structural characterization is presented in the Supplemental Material [47].

Interestingly, the r-222 peak splits into two sets of 022 and 402 orthorhombic peaks at the same 2θ but at different ω positions. This twining arises due to the symmetry equivalent $AFM^2_{[1\bar{1}0]}$ spin alignment along two different directions $[1\bar{1}0]$ and [110] [Fig. S9]. The magnetic stress during the rocksalt-to-orthorhombic structural transition occurs along both the $[1\bar{1}0]$ and [110] directions, which results in orthorhombic CrN grains with the same crystal symmetry but different in-plane orientations. The observation of the twining during the phase transition itself points to the anisotropy of the magnetic stress that is predicted in theory [23].

Further careful observation of the XRD peaks reveals that the angular separation ($\Delta 2\theta$) between the orthorhombic 022 and 402 peaks broadens with the reduction in temperature (Figs. S11,S12 [47]). This broadening in angular separation with temperature results from the fact that, as the temperature is reduced, the AFM interaction between Cr atoms becomes stronger, intensifying the driving force. As a result, the orthorhombic lattice parameters a shrinks and b expand further with the reduction in temperature (Fig. S13 [47]), as predicted in theory [23,24]. Thereby, these combined electrical, magnetic, and structural characterizations strongly prove the anisotropic magnetic stress-driven metal-insulator transition in CrN.

To further engineer the magnetic exchange interactions, nonmagnetic cations magnesium (Mg) and aluminium (Al)

are introduced on the Cr site and ~240 nm $Cr_{0.96}Mg_{0.04}N$ and $Cr_{0.96}Al_{0.04}N$ solid-solution alloys are deposited on (001) MgO substrates. Temperature-dependent resistivity measurements (Figs. S24,S25 [47]) show that compared to the phase-pure CrN, $Cr_{0.96}Mg_{0.04}N$ and $Cr_{0.96}Al_{0.04}N$ exhibit a much lower MIT temperature of ~220 K, with a hysteresis temperature of ~2–3 K. Since the inclusion of nonmagnetic Mg and Al at Cr sites reduces the exchange interactions, the phase transition temperature also decreases accordingly. The structural transition of $Cr_{0.96}Mg_{0.04}N$ film is further determined with Raman spectroscopy measurement. Since the first-order Raman scattering is symmetry forbidden in the rocksalt structure, no Raman peak is observed in $Cr_{0.96}Mg_{0.04}N$ as the temperature is lowered from 350 to 220 K [Fig. S25(b) [47]]. However, below 220 K, as the structure transitions from rocksalt-to-orthorhombic, corresponding Raman peaks [43,48] started to appear.

Finally, the first-principle DFT calculations [52] of CrN with $AFM^2_{[1\bar{1}0]}$ spin configuration is performed to explain the experimental results. A Hubbard U correction of 4.5 eV for the Cr d electrons is utilized to account for the onsite Coulomb interactions (A detailed discussion on computational method is included in Supplemental Material [47].). Band structure and density of states calculation show a tiny indirect gap of 0.2 eV in CrN [Fig. 4(a), S27 [47]], consistent with the earlier reports [37,53,54]. Cr-Cr nearest-neighbour AFM exchange-energy of −10.6 meV is calculated in the relaxed configuration [55]. The exchange-interaction energy (J_1) increases linearly when compressive-strain is considered and decreases when tensile-strain is considered in theoretical modeling [Fig. 4(b)].

After the theoretical calculation, the obtained J_1 value is used in spin dynamics simulation [56] to calculate the magnetic susceptibility and specific heat across the T_N [Figs. 4(c) and 4(d)]. The sharp peak in the temperature-dependent susceptibility and specific heat corresponds to the T_N. The calculated T_N of unstrained CrN appears at ~290 K, slightly higher than the measured phase transition temperature of ~278 K. However, when compressive and tensile strain is considered in the calculations, the shift in the T_N follows the same trend as experimental observations, which verifies the underlying magnetic stress-driven phase transition mechanism.

In conclusion, our work presents conclusive experimental evidence about the existence and manipulation of the magnetic stress-driven metal-insulator phase transition. This mechanism contrasts with the strong Coulomb repulsion or Peierls instability-driven metal-insulator phase transition that most conventional materials exhibit. Furthermore, demonstration of the room temperature metal-insulator phase transition in prototype CrN by tuning the magnetic stress would enable the practical utilization of the transition phenomena in ambient conditions. Therefore, this work marks a paradigm shift in the physical origin of the metal-insulator phase transition mechanism and will open up a new research direction to study the coupled magneto-structural-electrical phase transition phenomena in magnetic semiconductors. We believe this will also broaden the choice of materials exhibiting metal-insulator transitions by introducing new classes of materials beyond oxides and sulfides.

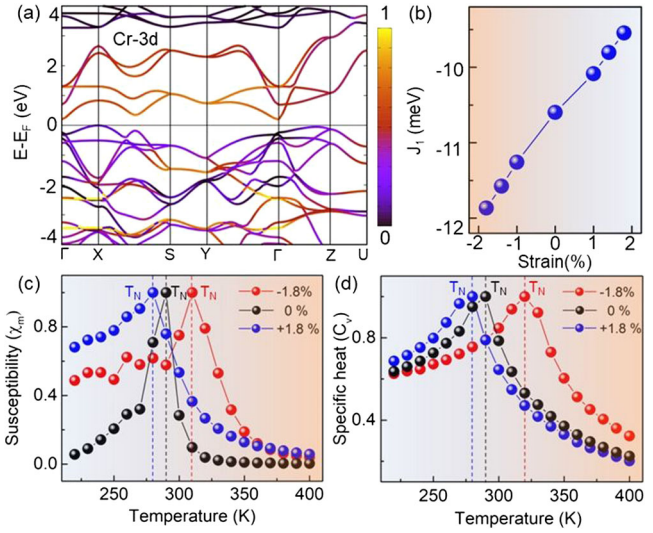

FIG. 4. (a) Cr-3d orbital contribution to the electronic structure of CrN. (b) Changes in antiferromagnetic exchange interaction energy (J_1) with epitaxial strain. J_1 increases for the compressive strain and decreases for the tensile strain. Spin dynamics simulation of magnetic susceptibility (χ_m) (c), and specific heat (C_v) (d) with temperature. The sharp peak in the plot corresponds to the T_N.

B. B., S. R., and B. S. acknowledge ICMS and SSL in JNCASR for support. B. S. acknowledges Young Scientist Research Award (YSRA) from the Board of Research in Nuclear Sciences, Department of Atomic Energy, India with Grant No. 59/20/10/2020-BRNS/59020 for financial support. M. G. and A. I. K. P. acknowledge the facilities of Sydney Microscopy and Microanalysis at The University of Sydney. Financial support by the DST provided within the framework of the India@DESY collaboration (Proposal No. I-20210384) is gratefully acknowledged. T. M. and M. B. acknowledge the Science and Engineering Research Board (Grant SERB-SRG 2021/000423), and the Prime Minister's Research Fellowship. M. d H. and J. L. M.-D. thank the European Union's Horizon 2020 research and innovation programme BeMAGIC under the Marie Sklodowska-Curie Grant Agreement No. 861145. J. L. M.-D. and T. M. acknowledge support from the Royal Academy of Engineering Chair in Emerging Technologies Grant CiET1819\24, and the European Research Council ERC Advanced (Grant Agreement EU-H2020-ERC-ADG #882929), EROS. S. R. acknowledges Mr. Xu He for the helpful discussion. B. S. acknowledges Professor Junqiao Wu (UC Berkeley) for helpful discussions.

B. B. and B. S. conceived this project. B. B. deposited the thin films. B. B. and S. A. performed the electrical measurements. S. R. and B. S. performed the theoretical modeling. A. I. K. P. performed the TEM sample preparation and M. G. performed the TEM imaging and analysis. A. J. and C. N. performed the Raman spectroscopy measurements and analysis. A. B. D. and F. B. performed the HRXRD measurements at DESY. N. P. and R. S. R. deposited the FM/AFM bilayer film. M. B., M. d H., J. D., and T. M. performed magnetic measurements and EB study. D. P. P. performed magnetoresistance measurement. All authors discussed and contributed to the preparation of the manuscript.

*To whom all correspondence should be addressed: bsaha@jncasr.ac.in and bivas.mat@gmail.com

[1] E. J. W. Verwey, Electronic conduction of magnetite (Fe_3O_4) and its transition point at low temperatures, Nature (London) **144**, 327 (1939).

[2] N. F. Mott, Metal-insulator transition, Rev. Mod. Phys. **40**, 677 (1968).

[3] R. Peierls and R. E. Peierls, *Quantum Theory of Solids* (Oxford University Press, New York, 1955).

[4] M. Imada, A. Fujimori, and Y. Tokura, Metal-insulator transitions, Rev. Mod. Phys. **70**, 1039 (1998).

[5] K. Liu, S. Lee, S. Yang, O. Delaire, and J. Wu, Recent progresses on physics and applications of vanadium dioxide, Mater. Today **21**, 875 (2018).

[6] K. Liu, C. Cheng, Z. Cheng, K. Wang, R. Ramesh, and J. Wu, Giant-amplitude, high-work density microactuators with phase transition activated nanolayer bimorphs, Nano Lett. **12**, 6302 (2012).

[7] R. M. Wentzcovitch, W. W. Schulz, and P. B. Allen, VO_2: Peierls or Mott-Hubbard? A View from Band Theory, Phys. Rev. Lett. **72**, 3389 (1994).

[8] R. Eguchi, M. Taguchi, M. Matsunami, K. Horiba, K. Yamamoto *et al.*, Photoemission evidence for a Mott-Hubbard metal-insulator transition in VO_2, Phys. Rev. B **78**, 075115 (2008).

[9] Z. Zinamon and N. F. Mott, Metal-non-metal transitions in narrow band materials; crystal structure versus correlation, Philos. Mag. **21**, 881 (1970).

[10] E. Abrahams, *50 Years of Anderson Localization* (World Scientific, Singapore, 2010), Vol. 24, 10.1142/7663.

[11] S. van Smaalen, The peierls transition in low-dimensional electronic crystals, Acta Crystallogr. Sect. A **61**, 51 (2005).

[12] S. S. Kondov, W. R. McGehee, J. J. Zirbel, and B. DeMarco, Three-dimensional Anderson localization of ultracold matter, Science (1979) **334**, 66 (2011).

[13] J. Chabé, G. Lemarié, B. Grémaud, D. Delande, P. Szriftgiser, and J. C. Garreau, Experimental Observation of the Anderson Metal-Insulator Transition with Atomic Matter Waves, Phys. Rev. Lett. **101**, 255702 (2008).

[14] M. J. Wahila, G. Paez, C. N. Singh, A. Regoutz, S. Sallis *et al.*, Evidence of a second-order peierls-driven metal-insulator transition in crystalline NbO_2, Phys. Rev. Mater. **3**, 074602 (2019).

[15] F. J. Morin, Oxides Which Show a Metal-to-Insulator Transition at the Néel Temperature, Phys. Rev. Lett. **3**, 34 (1959).

[16] S. Kumar, J. P. Strachan, M. D. Pickett, A. Bratkovsky, Y. Nishi, and R. S. Williams, Sequential electronic and structural transitions in VO_2 observed using x-ray absorption spectromicroscopy, Adv. Mater. **26**, 7505 (2014).

[17] R. Zhang, Q. S. Fu, C. Y. Yin, C. L. Li, X. H. Chen, G. Y. Qian, C. L. Lu, S. L. Yuan, X. J. Zhao, and H. Z. Tao, Understanding of metal-insulator transition in VO_2 based on experimental and theoretical investigations of magnetic features, Sci. Rep. **8**, 17093 (2018).

[18] B. A. Frandsen, Y. Kalcheim, I. Valmianski, A. S. McLeod, Z. Guguchia *et al.*, Intertwined magnetic, structural, and electronic transitions in V_2O_3, Phys. Rev. B **100**, 235136 (2019).

[19] M. Yang *et al.*, Suppression of structural phase transition in VO_2 by epitaxial strain in vicinity of metal-insulator transition, Sci. Rep. **6**, 23119 (2016).

[20] D. Meyers *et al.*, Pure electronic metal-insulator transition at the interface of complex oxides, Sci. Rep. **6**, 27934 (2016).

[21] D. Lee *et al.*, Isostructural metal-insulator transition in VO_2, Science (1979) **362**, 1037 (2018).

[22] L. Casillas-Trujillo, R. Armiento, and B. Alling, Identification of materials with strong magnetostructural coupling using computational high-throughput screening, Phys. Rev. Mater. **5**, 034417 (2021).

[23] A. Filippetti and N. A. Hill, Magnetic Stress as a Driving Force of Structural Distortions: The Case of CrN, Phys. Rev. Lett. **85**, 5166 (2000).

[24] A. Filippetti, W. E. Pickett, and B. M. Klein, Competition between magnetic and structural transitions in CrN, Phys. Rev. B **59**, 7043 (1999).

[25] I. Stockem, A. Bergman, A. Glensk, T. Hickel, F. Körmann, B. Grabowski, J. Neugebauer, and B. Alling, Anomalous Phonon Lifetime Shortening in Paramagnetic CrN Caused by Spin-Lattice Coupling: A Combined Spin and *Ab Initio* Molecular Dynamics Study, Phys. Rev. Lett. **121**, 125902 (2018).

[26] J. Zemen, Z. Gercsi, and K. G. Sandeman, Piezomagnetism as a counterpart of the magnetovolume effect in magnetically frustrated mn-based antiperovskite nitrides, Phys. Rev. B **96**, 024451 (2017).

[27] J. L. Garca-Muñoz, J. Rodriguez-Carvajal, P. Lacorre, and J. B. Torrance, Neutron-diffraction study of RNiO3 (R = La,Pr,Nd,Sm): Electronically induced structural changes across the metal-insulator transition, Phys. Rev. B **46**, 4414 (1992).

[28] D. Adler, Mechanisms for metal-nonmental transitions in transition-metal oxides and sulfides, Rev. Mod. Phys. **40**, 714 (1968).

[29] G. M. Abramova and G. A. Petrakovskii, Metal-insulator transition, magnetoresistance, and magnetic properties of 3d-sulfides (review), Low Temp. Phys. **32**, 725 (2006).

[30] B. Alling, T. Marten, and I. A. Abrikosov, Effect of magnetic disorder and strong electron correlations on the thermodynamics of CrN, Phys. Rev. B **82**, 184430 (2010).

[31] L. M. Corliss, N. Elliott, and J. M. Hastings, Antiferromagnetic structure of CrN, Phys. Rev. **117**, 929 (1960).

[32] A. Ney, R. Rajaram, S. S. P. Parkin, T. Kammermeier, and S. Dhar, Magnetic properties of epitaxial CrN films, Appl. Phys. Lett. **89**, 112504 (2006).
[33] C. Constantin, M. B. Haider, D. Ingram, and A. R. Smith, Metal/semiconductor phase transition in chromium nitride(001) grown by Rf-plasma-assisted molecular-beam epitaxy, Appl. Phys. Lett. **85**, 6371 (2004).
[34] Q. Jin *et al.*, Anisotropic electronic phase transition in CrN epitaxial thin films, Appl. Phys. Lett. **120**, 73103 (2022).
[35] P. A. Bhobe, A. Chainani, M. Taguchi, T. Takeuchi, R. Eguchi *et al.*, Evidence for a Correlated Insulator to Antiferromagnetic Metal Transition in CrN, Phys. Rev. Lett. **104**, 236404 (2010).
[36] B. Alling, T. Marten, and I. A. Abrikosov, Questionable collapse of the bulk modulus in CrN, Nat. Mater. **9**, 283 (2010).
[37] A. Herwadkar and W. R. L. Lambrecht, Electronic structure of CrN: A borderline Mott insulator, Phys. Rev. B **79**, 035125 (2009).
[38] J. D. Browne, P. R. Liddell, R. Street, and T. Mills, An investigation of the antiferromagnetic transition of CrN, Phys. Status Solidi (a) **1**, 715 (1970).
[39] R. M. Ibberson and R. Cywinski, The magnetic and structural transitions in CrN and (CrMo)N, Physica (Amsterdam) **180–181B**, 329 (1992).
[40] Q. Jin *et al.*, Strain-mediated high conductivity in ultrathin antiferromagnetic metallic nitrides, Adv. Mater. **33**, 2005920 (2021).
[41] X. Y. Zhang, J. S. Chawla, R. P. Deng, and D. Gall, Epitaxial suppression of the metal-insulator transition in CrN, Phys. Rev. B **84**, 073101 (2011).
[42] X. F. Duan, W. B. Mi, Z. B. Guo, and H. L. Bai, A comparative study of transport properties in polycrystalline and epitaxial chromium nitride films, J. Appl. Phys. **113**, 23701 (2013).
[43] B. Biswas, S. Chakraborty, A. Joseph, S. Acharya, A. I. K. Pillai, C. Narayana, V. Bhatia, M. Garbrecht, and B. Saha, Secondary phase limited metal-insulator phase transition in chromium nitride thin films, Acta Mater. **227**, 117737 (2022).
[44] B. Biswas, S. Chakraborty, O. Chowdhury, D. Rao, A. I. K. Pillai, V. Bhatia, M. Garbrecht, J. P. Feser, and B. Saha, In-plane Cr_2N-CrN metal-semiconductor heterostructure with improved thermoelectric properties, Phys. Rev. Mater. **5**, 114605 (2021).
[45] P. Subramanya Herle, M. S. Hegde, N. Y. Vasathacharya, S. Philip, M. V Rama Rao, and T. Sripathi, Synthesis of TiN, VN, and CrN from ammonolysis of TiS_2, VS_2, and Cr_2S_3, J. Solid State Chem. **134**, 120 (1997).
[46] M. A. Gharavi *et al.*, Microstructure and thermoelectric properties of CrN and CrN/Cr_2N thin films, J. Phys. D Appl. Phys. **51**, 355302 (2018).
[47] See Supplemental Material at http://link.aps.org/supplemental/10.1103/PhysRevLett.131.126302 for details about experimental and computational methods and additional results.
[48] C. X. Quintela *et al.*, Epitaxial CrN thin films with high thermoelectric figure of merit, Adv. Mater. **27**, 3032 (2015).
[49] T. Maity, S. Goswami, D. Bhattacharya, and S. Roy, Superspin Glass Mediated Giant Spontaneous Exchange Bias in a Nanocomposite of $BiFeO_3$-$Bi_2Fe_4O_9$, Phys. Rev. Lett. **110**, 107201 (2013).
[50] J. C. Lin, B. S. Wang, P. Tong, W. J. Lu, L. Zhang, X. B. Zhu, Z. R. Yang, W. H. Song, J. M. Dai, and Y. P. Sun, AlN_xMn_3: A possible high-temperature soft magnetic material and strongly correlated system, Appl. Phys. Lett. **98**, 92507 (2011).
[51] O. H. Seeck *et al.*, The high-resolution diffraction beamline P08 At ~ PETRA III, J. Synchrotron Radiat. **19**, 30 (2012).
[52] P. Giannozzi *et al.*, QUANTUM ESPRESSO: A modular and open-source software project for quantum of materials, J. Phys. Condens. Matter **21**, 395502 (2009).
[53] A. S. Botana, F. Tran, V. Pardo, D. Baldomir, and P. Blaha, Electronic structure of CrN: A comparison between different exchange correlation potentials, Phys. Rev. B **85**, 235118 (2012).
[54] T. Rojas and S. E. Ulloa, Strain fields and electronic structure of antiferromagnetic CrN, Phys. Rev. B **96**, 125203 (2017).
[55] X. He, N. Helbig, M. J. Verstraete, and E. Bousquet, TB2J: A PYTHON package for computing magnetic interaction parameters, Comput. Phys. Commun. **264**, 107938 (2021).
[56] X. Gonze *et al.*, The Abinitproject: Impact, environment and recent developments, Comput. Phys. Commun. **248**, 107042 (2020).